

Field enhanced electron mobility by nonlinear phonon scattering of Dirac electrons in semiconducting graphene nanoribbons

Danhong Huang,¹ Godfrey Gumbs,² and O. Roslyak²

¹*Air Force Research Laboratory, Space Vehicles Directorate,
Kirtland Air Force Base, NM 87117, USA and*

²*Department of Physics and Astronomy,
Hunter College of the City University of New York,
695 Park Avenue, New York, NY 10065, USA*

(Dated: February 1, 2011)

Abstract

The calculated electron mobility for a graphene nanoribbon as a function of applied electric field has been found to have a large threshold field for entering a nonlinear transport regime. This field depends on the lattice temperature, electron density, impurity scattering strength, nanoribbon width and correlation length for the line-edge roughness. An enhanced electron mobility beyond this threshold has been observed, which is related to the initially-heated electrons in high energy states with a larger group velocity. However, this mobility enhancement quickly reaches a maximum due to the Fermi velocity in graphene and the dramatically increased phonon scattering. Super-linear and sub-linear temperature dependence of mobility seen in the linear and nonlinear transport regimes. By analyzing the calculated non-equilibrium electron distribution function, this difference is attributed separately to the results of sweeping electrons from the right Fermi edge to the left one through the elastic scattering and moving electrons from low-energy states to high-energy ones through field-induced electron heating. The threshold field is pushed up by a decreased correlation length in the high field regime, and is further accompanied by a reduced magnitude in the mobility enhancement. This implies an anomalous high-field increase of the line-edge roughness scattering with decreasing correlation length due to the occupation of high-energy states by field-induced electron heating.

I. INTRODUCTION

The engineering achievement of isolating graphene sheets¹⁻³ from graphite has inspired many studies aimed at understanding basic underlying physics^{1,4} as well as finding possible applications to carbon-based electronics⁵. The linear transport of charge carriers in a graphene layer, has received a considerable amount of attention.⁶⁻¹² Recent reports on the successful fabrications of ultra-fast graphene transistors¹³ and photodetector¹⁴ have further pushed this research frontier into the fields of electronics and optoelectronics. However, similar studies of linear transport in graphene nanoribbons (GNRs) has only been given relatively little attention so far.¹⁵⁻¹⁷

Early theoretical studies^{11,16} on electron transport in graphene nanoribbons were restricted to the low-field limit, where a linearized Boltzmann equation was solved within a relaxation-time approximation. In this paper, the non-equilibrium distribution of electrons is calculated exactly by solving the Boltzmann equation beyond the relaxation-time approximation for nonlinear electron transport in semiconducting graphene nanoribbons. Enhanced electron mobility from initially-heated electrons in high energy states is anticipated. An anomalous increase in the line-edge roughness scattering for large electric fields is obtained with decreasing roughness correlation length due to the occupation of high-energy states by field-induced electron heating. Although the numerical results in this paper are given only for semiconducting graphene nanoribbons, the derived formalism here can also be applied to metallic graphene nanoribbons by formally taking the limit $W \rightarrow \infty$. The semi-classical Boltzmann transport equation is expected to be applicable to the diffusive band-transport regime with relative smooth edges for graphene nanoribbons, instead of the hopping and tunneling between localized states with rough edges.

The rest of the paper is organized as follows. In Sec. II, we exactly solve the semi-classical Boltzmann equation for low-temperature electron transport in semiconducting graphene nanoribbons by including impurity, line-edge roughness and phonon scattering effects at a microscopic level. Based on the calculated non-equilibrium distribution as a function of wave number along the ribbon, we present detailed numerical results for electron mobility as a function of either the applied electric field or the lattice temperature for various electron densities, impurity scattering strengths, nanoribbon widths and correlation lengths for line-edge roughness. The conclusions deduced from these results are briefly summarized in Sec.

III.

II. MODEL AND THEORY

We restrict ourselves to single subband transport. Low electron densities, moderate temperatures, ionized impurities and line-edge roughness are assumed^{16,18,19}. Therefore, negligible effects of electron-electron²⁰, optical phonon¹⁹, inter-valley and volume-distributed impurity scattering¹⁶ will be ignored. Typical armchair nanoribbon (ANR) configuration is shown in Fig. 1. The electron-like dispersion equation branch for ANR can be represented on a k -mesh as⁴

$$\varepsilon_j = \hbar\nu_F \times \begin{cases} k_j & \text{metallic} \\ \sqrt{k_j^2 + (\pi/3W)^2} & \text{semiconducting} \end{cases}. \quad (1)$$

Here, $\nu_F = 10^8$ cm/s is the Fermi velocity in graphene. The wave numbers $k_j = [j - (N + 1)/2] \delta k$ are given on the discrete mesh $j = 1, 2, \dots, N$ for large odd integer N . $\delta k = 2k_{\max}/(N - 1)$ is a small mesh spacing. k_{\max} is chosen so that scattering induced population of higher electron-like branches may be neglected (see Fig. 1). The minimum in the dispersion curve corresponds to the central mesh point $j = M = (N + 1)/2$. Also, $W = (\mathcal{N} + 1)a_0/2$ is the width of the ribbon expressed in units of the size of the graphene unit cell $a_0 = 2.6 \text{ \AA}$ and number of carbon atoms across the ribbon \mathcal{N} . According to the dispersion relation in Eq. (1), the electron group velocity v_j for metallic nanoribbons on the first subband is determined by the Fermi velocity ν_F , while for semiconducting ANRs, it assumes the form $v_j = \nu_F (\hbar\nu_F k_j / \varepsilon_j)$. We shall also assume that the electron-like branch is filled up to $|k_j| = k_F$ at zero temperature with the Fermi wave number and energy given by $k_F = \pi n_{1D}/2$ and $\varepsilon_F = \varepsilon(k_F)$, which can be applied to both metallic and semiconducting graphene nanoribbons by choosing the zero energy at the subband edge. For a chosen temperature T and chemical potential μ_0 , the linear electron density in ANR follows from $n_{1D} = \delta k / \pi \sum_{j=1}^N [\exp((\varepsilon_j - \mu_0)/k_B T) + 1]^{-1}$.

The wave function $\Psi_j(x, y)$ corresponding to the energy in Eq. (1) must satisfy hard-wall boundary conditions²¹ $\Psi_j(0, y) = \Psi_j(W, y) = 0$. This can be assured by choosing the wave function as a mixture of those at $\mathbf{K} = (2\pi/3a_0, 2\pi/\sqrt{3}a_0)$ and $\mathbf{K}' = (-2\pi/3a_0, 2\pi/\sqrt{3}a_0)$ points as⁴

$$\Psi_j(x, y) = \frac{1}{\sqrt{2}} [\psi_j(x, y) - \psi'_j(x, y)] , \quad (2)$$

$$\begin{cases} \psi_j(x, y) = \sqrt{\frac{1}{2LW}} e^{ik_j y} \begin{bmatrix} 1 \\ e^{i\phi_j} \end{bmatrix} e^{i(2\pi/3a_0 - \kappa)x} & \text{at } \mathbf{K} \text{ point} \\ \psi'_j(x, y) = \sqrt{\frac{1}{2LW}} e^{ik_j y} \begin{bmatrix} 1 \\ -e^{-i\phi_j} \end{bmatrix} e^{-i(2\pi/3a_0 - \kappa)x} & \text{at } \mathbf{K}' \text{ point} \end{cases} . \quad (3)$$

Here, L is the quantization length of the ribbon. For semiconducting ANR $\kappa = \pi/3W \ll 2\pi/3a_0$ is the quanta of the transverse wave vector. $\phi_j = \tan^{-1}(k_j/\kappa)$ is the phase separation between the two graphene sublattices. For metallic type of = ribbon, we have $\kappa = 0$ and the phase assumes only $\pm\pi/2$ values.

Given the wave function in Eq. (2) and neglecting effects due to inter-valley scattering²² one can calculate the scattering from any given potential $V(x, y)$. The impurity and phonon induced inter-valley scattering has been ignored based on the assumption that the required momentum transfer is relative large in comparison with the low-temperature phonon energies as well as the suppressed effective scattering cross section of both volume and surface impurities for very large value $|\mathbf{K} - \mathbf{K}'|$. Corresponding interaction matrix elements are

$$V_{i,j} = \int_0^W dx \int_{-\infty}^{\infty} dy \Psi_i^*(x, y) V(x, y) \Psi_j(x, y) = \frac{1}{2} \int_0^W dx \int_{-\infty}^{\infty} dy (\psi_i^* V \psi_j + \psi_i'^* V \psi_j') . \quad (4)$$

Our model accounts for the net scattering potential made from the three components $V = V^{\text{AL}} + V^{\text{LER}} + V^{\text{imp}}$.

The longitudinal mode considered in this paper induces higher deformation potential than the out-of-plane flexural modes, and we neglect the transverse flexural modes here as a leading-order approximation. In this approximation, the inelastic scattering is provided only by longitudinal acoustic phonons. The perturbation potential induced by them is given by^{16,23}

$$V^{\text{AL}}(y) = \sqrt{\frac{n^{\pm}\hbar}{2\rho LW\omega_{\text{AL}}}} D_{\text{AL}} q_y e^{iq_y y} , \quad (5)$$

where the phonon distributions are $n^- = [\exp(\hbar\omega_{AL}/k_B T) - 1]^{-1}$, $n^+ = 1 + n^-$, T is the temperature, $\omega_{AL} = c_s q_y$ is the phonon frequency, $D_{AL} \sim 16$ eV is the deformation potential, $\rho \sim 7.6 \times 10^{-8}$ g/cm² and $c_s \sim 2 \times 10^6$ cm/s are the mass density and sound velocity in graphene. Also, one has to assure momentum conservation during scattering, i.e., $q_y = k_i - k_j$.

Elastic scattering is due to the roughness of the ribbon edges as well as in-plane charged impurities. To model the first we shall assume that the width of the ribbon has the form $W(y) = W + \delta W(y)$, where the edge-roughness is assumed to satisfy Gaussian correlation function $\langle \delta W(y) \delta W(y + \Delta y) \rangle = \delta b^2 \exp[-(\Delta y/\Lambda_0)^2]$ with $\delta b \sim 5$ Å being the amplitude and $\Lambda_0 \sim 50 - 200$ Å being the correlation length of the roughness. The second mechanism is given by impurities located at $(x_0, 0, 0)$ and distributed with a sheet density n_{2D} . Each of the point impurities provide the scattering Coulomb potential. Since the momentum difference between two valleys is rather large, $|\mathbf{K} - \mathbf{K}'| = 4\pi/3a$, only short-range impurities (such as topological defects) with a range smaller than the lattice constant causes inter-valley scattering. In contrast, for wide enough ribbons with uniformly distributed long-range impurities (such as charged defects) the scattering processes is restricted to intra-valley scattering^{24,25}. Here we neglect the short range scatterers in favor of the charged impurities thus making the scattering matrix diagonal with all elements given by Eq.(7). Such simplification has been invoked in order to keep the conventional part of the Boltzmann transport equation as simple as possible and focus on the nonlinear counterpart. Corresponding perturbations for roughness and impurity scattering are given by

$$V^{\text{LER}}(y) = \frac{\delta W(y)}{3W^2} \pi \hbar \nu_F, \quad (6)$$

$$V^{\text{imp}}(x, y) = \frac{e^2}{4\pi\epsilon_0\epsilon_r \sqrt{(x - x_0)^2 + y^2}}, \quad (7)$$

where ϵ_r is the average dielectric constant of the host. These potentials give rise to the net elastic scattering rate \hbar/τ_j on the k -mesh

$$\frac{1}{\tau_j} = \frac{1}{\tau_j^{imp}} + \frac{1}{\tau_j^{LER}} , \quad (8)$$

$$\begin{cases} (\tau_j^{imp})^{-1} = \gamma_0 \left(\frac{v_F}{|v_j|} \right) [1 + \cos(2\phi_j)] \\ (\tau_j^{LER})^{-1} = \gamma_1 \left(\frac{\nu_F}{|v_j|} \right) \frac{1}{1+4k_j^2\Lambda_0^2} [1 + \cos(2\phi_j)] \end{cases} , \quad (9)$$

where γ_0 denotes the impurity scattering rate at the Fermi edges and $\gamma_1 = 2 \left(\frac{\pi\nu_F\delta b}{3W^2} \right)^2 \frac{\Lambda_0}{\nu_F}$ is the scattering rate due to edge roughness. Here, we assume that the impurities lie within the graphene layer. The scattering rate will be modified for charged impurities in a substrate, which can be easily seen from the effective scattering cross section $\mathcal{S}(k_y, W)$ defined in Eq.(28) of Ref.[16]. Although this effect can be formally taken into account by varying the value of γ_0 in Eq.(9), the leading scattering mechanism is still provided by in-plane impurities. All the scattering potentials are screened by free carriers. Since we are limited to a single subband, the screening is described by the dielectric function. The inelastic scattering is shielded by the static Thomas-Fermi dielectric function in its general form^{16,26} $\epsilon_{TF}(|k_{j'} - k_j|)$. The screening of elastic scattering potentials is given by $\epsilon_{TF} \approx 1 + (e^2/\pi^2\epsilon_0\epsilon_r\hbar\nu_F)$ under the metallic limit ($2k_F W \gg 1$) with $\epsilon_r \approx 3.9$. We employ the static screening to both impurity and phonon scattering with electrons for the system with a relative large damping rate and small Fermi energy. The static screening tends to overestimate the scattering effect.²⁷ The dynamic screening effect on the electron scattering has been quantitatively evaluated within the RPA in a similar quantum-wire system,²⁷ and it becomes important whenever the damping energy is much smaller than the Fermi energy. The Fermi-golden rule has been employed to treat the leading contributions of both elastic and inelastic scattering. The multiple scattering effects are neglected due to low temperatures, low impurity densities and small line-edge roughness. Under application of a small electric field \mathcal{F}_0 along the GNR (see Fig. 1) the stationary current $I = (e\delta k/\pi) \sum_j f_j v_j$ establishes itself. It can be characterized by the electron mobility $\mu_e = I/en_{1D}\mathcal{F}_0$, where we have introduced the carrier distribution function partitioned as $f_j = f_j^{(0)} + g_j \approx f_j^{(0)} + b_j \tau_j^{TOT}$ with $f_j^{(0)} = \{1 + \exp[(\epsilon_j - \mu_c)/k_B T]\}^{-1}$ being the equilibrium Fermi-Dirac function, μ_c being the chemical potential of electrons, and $b_j = ev_j (\partial f_j^{(0)}/\partial \epsilon_j) \mathcal{F}_0$ being the drag. Such approximation for the distribution function is known as relaxation time approximation and

encompasses all (elastic and inelastic) scattering mechanisms into τ_j^{TOT} . The consequence of such an approximation is the electric field independent mobility and conductivity. However, by increasing \mathcal{F}_0 one may enter nonlinear regime when the conductivity and mobility become a function of the applied electric field. Studying of ANR in such nonlinear regime is the main subject of this work.

Formally, the deviation from the equilibrium Fermi distribution under strong electric field is described by the set of nonlinear reduced Boltzmann transport equations^{18,19}

$$\frac{dg'_j(t)}{dt} = b_j - \sum_{j' \neq M} a'_{j,j'}(t) g'_{j'}(t) , \quad (10)$$

In this notation, $g'_j(t) = g_j(t) - g_M(t)$ is the reduced form of the dynamical non-equilibrium part²⁸ of the electron distribution function. The reduced form accounts for particle number conservation condition, i.e., $\sum_{j=1}^N g_j(t) = 0$. The nonlinear reduced Boltzmann transport equations have been applied to study the electron dynamics in both quantum wires¹⁸ and quantum-dot superlattices¹⁹, where the full description on the derivation of the nonlinear reduced Boltzmann transport equations can be found. In the matrix Eq. (10), we introduced the matrix elements $a'_{j,j'}(t) = a_{j,j'}(t) - a_{j,M}(t)$ via its components

$$\begin{aligned} a_{j,j'}(t) &= \delta_{j,j'} \left[\mathcal{W}_j + \mathcal{W}_j^g(t) + \frac{1 - \delta_{j,(N+1)/2}}{2\tau_j} \right] - \delta_{j+j',N+1} \left[\frac{1 - \delta_{j,(N+1)/2}}{2\tau_j} \right] \\ &- \mathcal{W}_{j,j'} - \frac{e\mathcal{F}_0}{2\hbar\delta k} (\delta_{j,j'-1} - \delta_{j,j'+1}) . \end{aligned} \quad (11)$$

While the net elastic scattering rate is given by Eq. (8), the total inelastic rate assumes the form $\mathcal{W}_j = 1/\tau_j^{AL} = \sum_{j'} \mathcal{W}_{j,j'}$ with the scattering matrix given by

$$\mathcal{W}_{j,j'} = \frac{L}{2\pi} \delta k \sum_{\pm} \mathcal{W}_{j,j'}^{\pm} (n_{j,j'} + f_{j'}^{\pm}) \quad (12)$$

$$\mathcal{W}_{j,j'}^{\pm} = \theta(\pm\varepsilon_{j'} \mp \varepsilon_j) \left[\frac{D_{AL}^2 |\varepsilon_{j'} - \varepsilon_j|}{2\hbar^2 c_s^3 \rho L W \epsilon_{TF}^2 (|k_{j'} - k_j|)} \right] [1 + \cos(\phi_{j'} - \phi_j)] . \quad (13)$$

We have $f_j^- = f_j^{(0)}$, $f_j^+ = 1 - f_j^{(0)}$, $n_{j,j'} = N_0(|\varepsilon_{j'} - \varepsilon_j|/\hbar)$, $N_0(\omega_q) = [\exp(\hbar\omega_q/k_B T) - 1]^{-1}$ is the Bose function for thermal equilibrium phonons. Furthermore, the dynamical phonon scattering rate $\mathcal{W}_j^g(t)$ for nonlinear phonon scattering, which is also responsible for the

nonlinear electron transport and electron heating due to its dependence on $g'_{j'}(t)$, is in the form of

$$\mathcal{W}_j^g(t) = \frac{L}{2\pi} \delta k \sum_{j' \neq M} g'_{j'}(t) [\mathcal{W}_{j,j'}^+ - \mathcal{W}_{j,j'}^- - (\mathcal{W}_{j,M}^+ - \mathcal{W}_{j,M}^-)] . \quad (14)$$

Once the non-equilibrium part, $g'_j(t)$, of the total electron distribution function has been solved from Eq. (10), the transient drift velocity, $v_c(t)$, of the system can be calculated according to

$$v_c(t) = \left[\sum_{j=1}^N f_j^{(0)} \right]^{-1} \times \begin{cases} \sum_{j \neq M} (v_j - v_M) g'_j(t) , & \text{semiconducting} \\ 2\nu_F \sum_{j=1}^M g'_j(t) , & \text{metallic} \end{cases} . \quad (15)$$

It is noted that the thermal-equilibrium part of the electron distribution does not contribute to the drift velocity. The steady-state drift velocity v_d of electrons is given by $v_c(t)$ in the limit $t \rightarrow \infty$. Corresponding steady-state conduction current is given by $I = en_{1D}v_d$. The differential electron mobility for nonlinear transport is generalized to $\mu_e = \partial v_d / \partial \mathcal{F}_0$. Numerical simulation of these quantities in specific ANRs is the subject of the next section.

III. NUMERICAL RESULTS AND DISCUSSION

Figure 2(a) presents our calculated electron mobilities μ_e as a function of applied electric field \mathcal{F}_0 at $T = 10$ K (blue curve) and $T = 6$ K (red curve), respectively. Clearly, from Fig. 2(a), a strong \mathcal{F}_0 -dependence for μ_e appears at a lower value of \mathcal{F}_0 at higher temperature T in the nanoribbon. This \mathcal{F}_0 -dependent electron mobility μ_e has its physical origins in the dynamical electron-phonon scattering rate $\mathcal{W}_j^g(t)$ through its dependence on electron the distribution function given in Eq. (14). Consequently, it is reasonable to expect a lower threshold field, \mathcal{F}^* , for entering into a nonlinear transport regime ($\mathcal{F} > \mathcal{F}^*$) due to enhanced nonlinear phonon scattering at $T = 10$ K. The value of \mathcal{F}^* strongly depends on the parameters of the system, such as T , n_{1D} , γ_0 and Λ_0 , and an analytic expression for \mathcal{F}^* cannot be obtained in the nonlinear-transport regime. On the other hand, as $\mathcal{F}_0 \rightarrow 0$, μ_e is larger at $T = 10$ K than $T = 6$ K due to thermal population of high-energy states with a large electron group velocity. The initial decrease of μ_e with \mathcal{F}_0 is attributed to the gradual

increase of the frictional force from phonon scattering by \mathcal{F}_0 . At $T = 10$ K, μ_e is roughly independent of \mathcal{F}_0 below 0.75 kV/cm (linear regime). However, μ_e increases significantly with \mathcal{F}_0 above 0.75 kV/cm (nonlinear regime). Eventually, μ_e decreases with \mathcal{F}_0 once it exceeds 1.5 kV/cm (heating regime), leading to a saturation of the electron drift velocity. The electron group velocity $|v_j|$ increases with the wave number for small $|k_j|$ values, as can be seen from Eq. (1). However, the increase of $|v_j|$ slows down toward its upper limit ν_F provided $|k_j| \gg \pi/3W$ but still within the single-subband regime. The increase of μ_e with \mathcal{F}_0 in the nonlinear regime comes from the initially-heated electrons in high energy states with a larger group velocity, while the successive decrease of μ_e in the heating regime comes from the combination of the upper limit $v_j \leq \nu_F$ and the dramatically increased phonon scattering. In Fig. 2(b), the calculated electron drift velocities v_d are plotted as a functions of temperature when $\mathcal{F}_0 = 2$ kV/cm (blue curve) and $\mathcal{F}_0 = 1$ kV/cm (red curve). The fact that μ_e increases with T monotonically in both cases implies the electron scattering in two samples is not dominated by phonons but by impurities and line-edge roughness. Different behaviors in the increase of μ_e with temperature can be seen from Fig. 2(b) for linear and nonlinear electron transport. At $\mathcal{F}_0 = 2$ kV/cm for the high-field nonlinear transport, v_d (or μ_e) increases with T sub-linearly. On the other hand, v_d rises super-linearly with T for the low-field linear transport at $\mathcal{F}_0 = 1$ kV/cm. These different T dependence in μ_e for linear and nonlinear transports can be directly related to the non-equilibrium part of the electron distribution function g_j presented in Figs. 2(c) and 2(d). The calculated g_j (left scaled solid curves) at $T = 10$ K, as well as the total electron distribution function f_j (right scaled dashed curves), are shown in Fig. 2(c) as functions of electron wave number k_j along the ribbon when $\mathcal{F}_0 = 2$ kV/cm (blue curves) and $\mathcal{F}_0 = 1$ kV/cm (red curves). The electron heating may be visualized from Fig. 2(c) when $\mathcal{F}_0 = 2$ kV/cm as a result of thermally driven electrons from low to high-energy states by heat generated from a frictional force²³ through nonlinear phonon scattering. On the other hand, when $\mathcal{F}_0 = 1$ kV/cm, electrons are only swept by elastic scattering from the right Fermi edge to the left Fermi edge, corresponding to linear transport. Figure 2(d) also allows a comparison between the calculated g_j (left-hand scaled solid curves) and f_j (right scaled dashed curves) with $\mathcal{F}_0 = 2$ kV/cm as functions of k_j at $T = 10$ K (blue curves) and $T = 6$ K (red curves). One may conclude from Fig. 2(d) that the nonlinear phonon scattering becomes important at $T = 10$ K, while the elastic scattering of electrons dominates at $T = 6$ K, similar to the explanation given for Fig. 2(c).

We present, in Fig. 3(a), our numerical results for μ_e as a function of \mathcal{F}_0 at $T = 10$ K for different electron densities $n_{1D} = 1.0 \times 10^5 \text{ cm}^{-1}$ (blue curve) and $n_{1D} = 0.8 \times 10^5 \text{ cm}^{-1}$ (red curve). As $\mathcal{F}_0 \rightarrow 0$, μ_e is slightly increased for a higher value of n_{1D} due to introducing high-energy occupied states with a large group velocity. It is further found from Fig. 3(a) that a low electron density produces a small \mathcal{F}^* in the system. This is due to the fact that a small minimum energy $\hbar\omega_q \approx 2\hbar c_s k_F$ is required for initializing phonon scattering in a low density sample, which enhances the nonlinear phonon scattering at a chosen temperature. However, the enhancement of μ_e due to \mathcal{F}_0 is large in a high density sample due to increased initial electron heating. In Fig. 3(b), v_d is presented at $\mathcal{F}_0 = 2 \text{ kV/cm}$ as a function of T for $n_{1D} = 1.0 \times 10^5 \text{ cm}^{-1}$ (blue curve) and $n_{1D} = 0.8 \times 10^5 \text{ cm}^{-1}$ (red curve). Although we still see μ_e increasing sub-linearly with T , as explained in Fig. 2(b), the rate of μ_e enhancement is large for a high- n_{1D} sample when T is not low, where the electron heating is significant. This observation is complemented by the results shown in Fig. 3(c), where electron heating becomes more significant for a high density sample although the nonlinear phonon scattering is seen to be important in both low and high density samples. This enhancement of μ_e with T at high electron densities is due to more low-energy electrons being available for thermal excitation to occupy high-energy states through electron heating.

The effects due to impurity scattering are compared in Figs. 4(a)-(c). In Fig. 4(a), we present a comparison of mobilities as a function of \mathcal{F}_0 at $T = 10$ K for $\gamma_0 = 1.0 \times 10^{13} \text{ s}^{-1}$ (blue curve) and $\gamma_0 = 1.0 \times 10^{14} \text{ s}^{-1}$ (red curve). As $\mathcal{F}_0 \rightarrow 0$, μ_e is greatly reduced by strong impurity scattering with $\gamma_0 = 1.0 \times 10^{14} \text{ s}^{-1}$ in the linear regime. In addition, for $\gamma_0 = 1.0 \times 10^{14} \text{ s}^{-1}$, \mathcal{F}^* is pushed upward from about 0.75 kV/cm to a higher value at 1.75 kV/cm , leaving us with a roughly \mathcal{F}_0 -independent μ_e in this case for the whole field range shown in this figure. The comparison for T -dependence of μ_e is presented in Fig. 4(b) for $\mathcal{F}_0 = 2 \text{ kV/cm}$, where a sub-linear increase of μ_e with T for weak impurity scattering is switched to a super-linear relation in the strong impurity scattering case. The effect of impurity scattering can also be seen from the calculated g_k and f_k as functions of k at $T = 10$ K and $\mathcal{F}_0 = 2 \text{ kV/cm}$ in Fig. 4(c), where the electron heating with $\gamma_0 = 1.0 \times 10^{13} \text{ s}^{-1}$ through nonlinear phonon scattering is completely masked by the strong impurity scattering at $\gamma_0 = 1.0 \times 10^{14} \text{ s}^{-1}$, leading to relative cooling of conduction electrons in a nanoribbon in the linear regime.

At relatively low temperatures $T \leq 10$ K and low concentration of electrons ($n_{1D} = 10^5 \text{ cm}^{-1}$) in the lowest conduction band, as well as medium impurity concentration $n_{2D} = 10^{10} \text{ cm}^{-2}$, the single conduction band approximation can be justified for graphene nanoribbons. Indeed, the energy separation between the first and second conduction subband is $\pi\hbar\nu_F/3W \approx 0.136 \text{ eV}$ for $W = 50 \text{ \AA}$. On the other hand, elastic and inelastic decay rate $\hbar\gamma_1 < \hbar\gamma_0 = 0.065 \text{ eV}$, as well as the Fermi energy $\varepsilon_F(\pi n_{1D}/2) \approx 0.01 \text{ eV}$, are much smaller.²⁹ More generally speaking, the model is valid provided that the scattering parameters and Fermi energy are of the order of the subband gap $E_g = 1.38/W \text{ eV}$ with W expressed in nanometers.

The increase of ribbon's width W will enlarge the electron group velocity $v_j < v_M \sim [1 + (2/3n_{1D}W)^2]^{-1/2}$, as shown by Eq. (1), and significantly decrease the effect of line-edge roughness scattering at the same time, as can be seen from the factor $\gamma_1 \sim (\pi\nu_F/3W)^2 (\delta b/W)^2$ in Eq. (9). Fixing $\Lambda_0 = 200 \text{ \AA}$ and making $\mathcal{F}_0 \rightarrow 0$, we do see from Fig. 5(a) that μ_e is dramatically increased when W is changed from 40 \AA ($\gamma_1 = 1.7 \times 10^{13} \text{ s}^{-1}$) to 50 \AA ($\gamma_1 = 4.28 \times 10^{13} \text{ s}^{-1}$) due to enlarged group velocity of electrons and reduced line-edge roughness scattering. In addition, the magnitude in the enhancement of μ_e with \mathcal{F}_0 is large in the sample with $W = 50 \text{ \AA}$ because the weakened elastic scattering, and therefore, the relatively strong initial heating of electrons by phonon scattering to high energy states with a larger group velocity. This is also reflected in the temperature dependence of v_d presented in Fig. 5(b). However, the rate for μ_e enhancement with T is almost the same in the two cases, implying a similar magnitude of nonlinear phonon scattering of electrons in both samples. This can be very well justified by the calculated g_j shown in Fig. 5(c), where the increase of W from 40 \AA to 50 \AA only slightly enhances the asymmetry of g_j with respect to $\pm k_j$, but the unique feature of electron heating is largely unchanged.

Finally, the effect of correlation length for the line-edge roughness on the transport is demonstrated in Figs. 6(a)-(c) by fixing $W = 50 \text{ \AA}$ and changing Λ_0 from 200 \AA to 50 \AA . As shown in Eq. (9), the line-edge roughness scattering can be either reduced or enhanced by decreasing Λ_0 , depending on $|k_j| \ll 1/2\Lambda_0$ or $|k_j| \gg 1/2\Lambda_0$. For our chosen sample with $n_{1D} = 1.0 \times 10^5 \text{ cm}^{-1}$, we find that the condition $|k_j| \ll 1/2\Lambda_0$ is satisfied in the low-field limit ($|k_j| \sim k_F$), while $|k_j| \gg 1/2\Lambda_0$ holds for the high field limit due to electron heating. Therefore, we find from Fig. 6(a) that μ_e is increased as $\mathcal{F}_0 \rightarrow 0$ when Λ_0 is reduced to 50 \AA in

the low field regime. However, the value of \mathcal{F}^* for μ_e is pushed upward for $\Lambda_0 = 50 \text{ \AA}$ in the high-field regime, which is further accompanied by a reduced magnitude in the enhancement of μ_e with \mathcal{F}_0 . This anomalous feature associated with reducing Λ_0 also has a profound impact on the T -dependence of μ_e as shown in Fig. 6(b), where the increasing rate of μ_e with T in the high field regime becomes much lower with $\Lambda_0 = 50 \text{ \AA}$ than for $\Lambda_0 = 200 \text{ \AA}$. In addition, the calculated g_j in Fig. 6(c) displays an anomalous cooling behavior (with a smaller spreading of f_j in the k_j space) in the high field regime for conduction electrons as Λ_0 is reduced to 50 \AA , similar to the results shown in Fig. 4(c).

We have performed similar calculations with metallic³⁰ ribbons of comparable width $W = 50 \pm 5 \text{ \AA}$ and found no perceptible difference in the nonlinear electron transport and heating provided that the rest of the parameters (electron and impurities concentrations and decay rates) are kept the same.

IV. CONCLUDING REMARKS

In conclusion, we have found there is a minimum electron mobility just before a threshold for an applied electric field when entering into the nonlinear transport regime, which is attributed to the gradual build-up of a frictional force from phonon scattering by the applied field. We also predict a field-induced mobility enhancement right after this threshold value, which is regarded as a consequence of initially-heated electrons in high energy states with a larger group velocity in an elastic-scattering dominated graphene nanoribbon. Moreover, we have discovered that this mobility enhancement reaches a maximum in the nonlinear transport regime as a combined result of an upper limit for the group velocity in a nanoribbon and a field-induced dramatically-increased phonon scattering in the system. Finally, the threshold field can be pushed upward and the magnitude in the mobility enhancement can be reduced simultaneously by a small correlation length for the line-edge roughness in the high-field limit due to the occupation of high-energy states by field-induced electron heating.

When the electron density is increased in a graphene nanoribbon, multi-subband transport occurs, the field-induced mobility enhancement is expected to be reduced, and the effect of electron-electron scattering needs to be included. When the lattice temperature becomes high, on the other hand, both the optical phonon and inter-valley scattering should

be considered. As the width of a nanoribbon is modulated, a periodic potential along the ribbon will form, leading to a graphene nanoribbon superlattice with additional miniband gap opening at the Brillouin zone boundaries. The results of the current research is expected to be very useful for the understanding and design of high-power and high-speed graphene nanoribbon emitters and detectors in the terahertz frequency range.

Acknowledgments

This research was supported by contract # FA 9453-07-C-0207 of AFRL. DH would like to thank the Air Force Office of Scientific Research (AFOSR) for its support.

-
- ¹ A. K. Geim and K. S. Novosolev, Nat. Mater. **6**, 183 (2007).
 - ² K. S. Novosolev, A. K. Geim, S. V. Morozov, D. Jiang, M. I. Katsnelson, I. V. Grigorieva, S. V. Dubonos, and A. A. Firsov, Nat. (London) **438**, 197 (2005).
 - ³ C. Berger, Z. Song, X. Li, X. Wu, N. Brown, C. Naud, D. Mayou, T. Li, J. Hass, A. N. Marchenkov, E. H. Conrad, P. N. First, and W. A. de Heer, Sci. **312**, 1191 (2006).
 - ⁴ A. H. C. Neto, F. Guinea, N. M. R. Peres, K. S. Nonoselov, and A. K. Geim, Rev. Mod. Phys. **81**, 109 (2009).
 - ⁵ P. Avouris, Z. Chen, and V. Perebeinos, Nat. Nanotechnol. **2**, 605 (2007).
 - ⁶ T. Ando, J. Phys. Soc. Jpn. **75**, 074716 (2006).
 - ⁷ J. H. Chen, C. Jang, S. Adam, M. S. Fuhrer, E. D. Williams, and M. Ishigami, Nat. Phys. **4**, 377 (2008).
 - ⁸ H. M. Dong, W. Xu, Z. Zeng, T. C. Lu, and F. M. Peeters, Phys. Rev. B **77**, 235402 (2008).
 - ⁹ N. M. R. Peres, J. M. B. Lopes dos Santos, and T. Stauber, Phys. Rev. B **76**, 073412 (2007); also see T. Stauber, N. M. R. Peres, and F. Guinea, *ibid.* **76**, 205423 (2007).
 - ¹⁰ V. V. Cheianov and V. I. Falko, Phys. Rev. Lett. **97**, 226801 (2006).
 - ¹¹ W. Xu, F. M. Peeters, and T. C. Lu, Phys. Rev. B **79**, 073403 (2009).
 - ¹² S. Y. Liu, X. L. Lei, and N. J. M. Horing, J. Appl. Phys. **104**, 043705 (2008).
 - ¹³ Y.-M. Lin, C. Dimitrakopoulos, K. A. Jenkins, D. B. Farmer, H.-Y. Chiu, A. Grill, and P. Avouris, Sci. **327**, 662 (2010).

- ¹⁴ T. Mueller, F. Xia, and P. Avouris, Nat. Photonics **4**, 297 (2010).
- ¹⁵ Y.-M. Lin, V. Perebeinos, Z. Chen, and P. Avouris, Phys. Rev. B **78** 161409 (2008).
- ¹⁶ T. Fang, A. Konar, H. Xing, and D. Jena, Phys. Rev. B **78**, 205403 (2008).
- ¹⁷ X. Wang, Y. Ouyang, X. Li, H. Wang, J. Guo, and H. Dai, Phys. Rev. Lett. **100**, 206803 (2008).
- ¹⁸ D. H. Huang and G. Gumbs, J. Appl. Phys. **107**, 103710 (2010).
- ¹⁹ D. H. Huang, S. K. Lyo and G. Gumbs, Phys. Rev. B **79**, 155308 (2009).
- ²⁰ S. K. Lyo and D. H. Huang, Phys. Rev. B **73**, 205336 (2006).
- ²¹ L. Brey and H. A. Fertig, Phys. Rev. B **73**, 235411(2006).
- ²² Such inter-valley scattering would require momentum transfer comparable with the distance between \mathbf{K} and \mathbf{K}' points.
- ²³ D. H. Huang, T. Apostolova, P. M. Alsing and D. A. Cardimona, Phys. Rev. B **69**, 075214 (2004).
- ²⁴ T. Ando and T. Nakanishi, J. Phys. Soc. Japan, **67**, 1704, (1998).
- ²⁵ K. Wakabayashi, Y. Takane, M. Yamamoto and M. Sigrist, New J. Phys. **11**, 095016, (2009).
- ²⁶ L. Brey and H. A. Fertig, Phys. Rev. B **75**, 125434 (2007).
- ²⁷ S. K. Lyo and D. H. Huang, Phys. Rev. B **66**, 155307 (2002).
- ²⁸ A distinct line must be drawn between equilibrium distribution function $f_j^{(0)}$ in absence of applied electric field and stationary solution of the transport equation $\lim_{t \rightarrow 0} f_j(t)$.
- ²⁹ $\hbar\gamma_1 < \hbar\gamma_0$ is valid for $\Lambda_0/W < 6$
- ³⁰ Two carbon atoms have been added/subtracted to the semiconducting ribbon across its width.

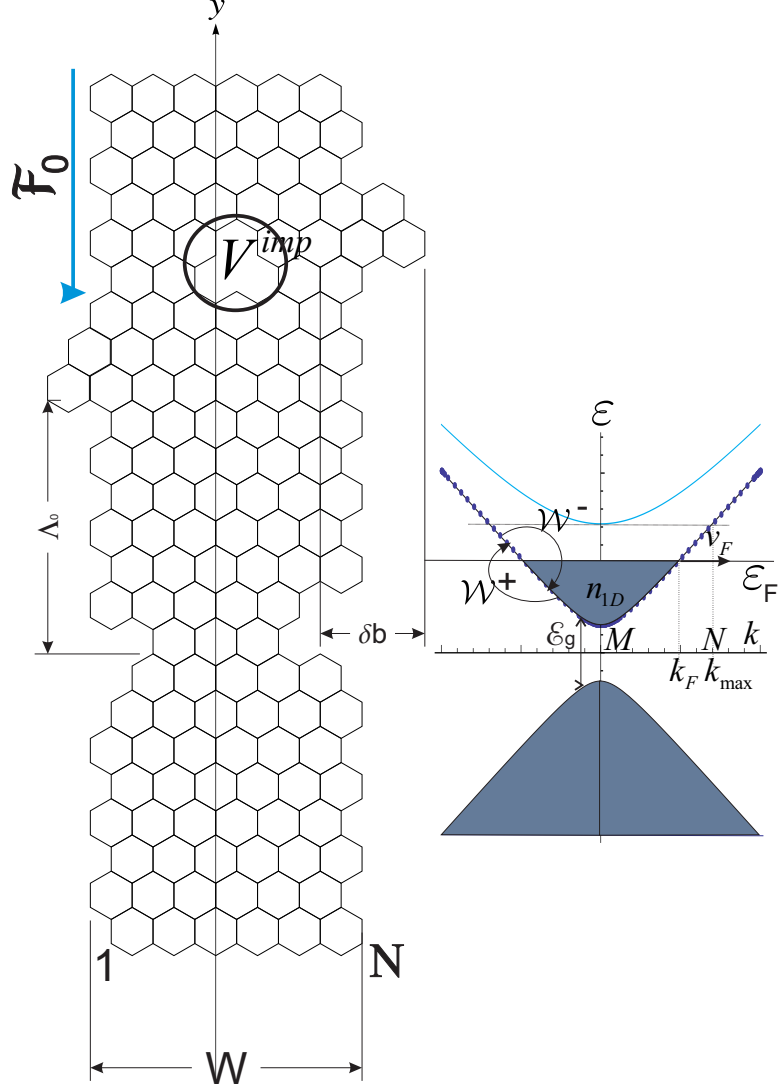


FIG. 1: Schematic illustration of the model employed in our numerical calculations. The parameters used in this figure are justified in the text.

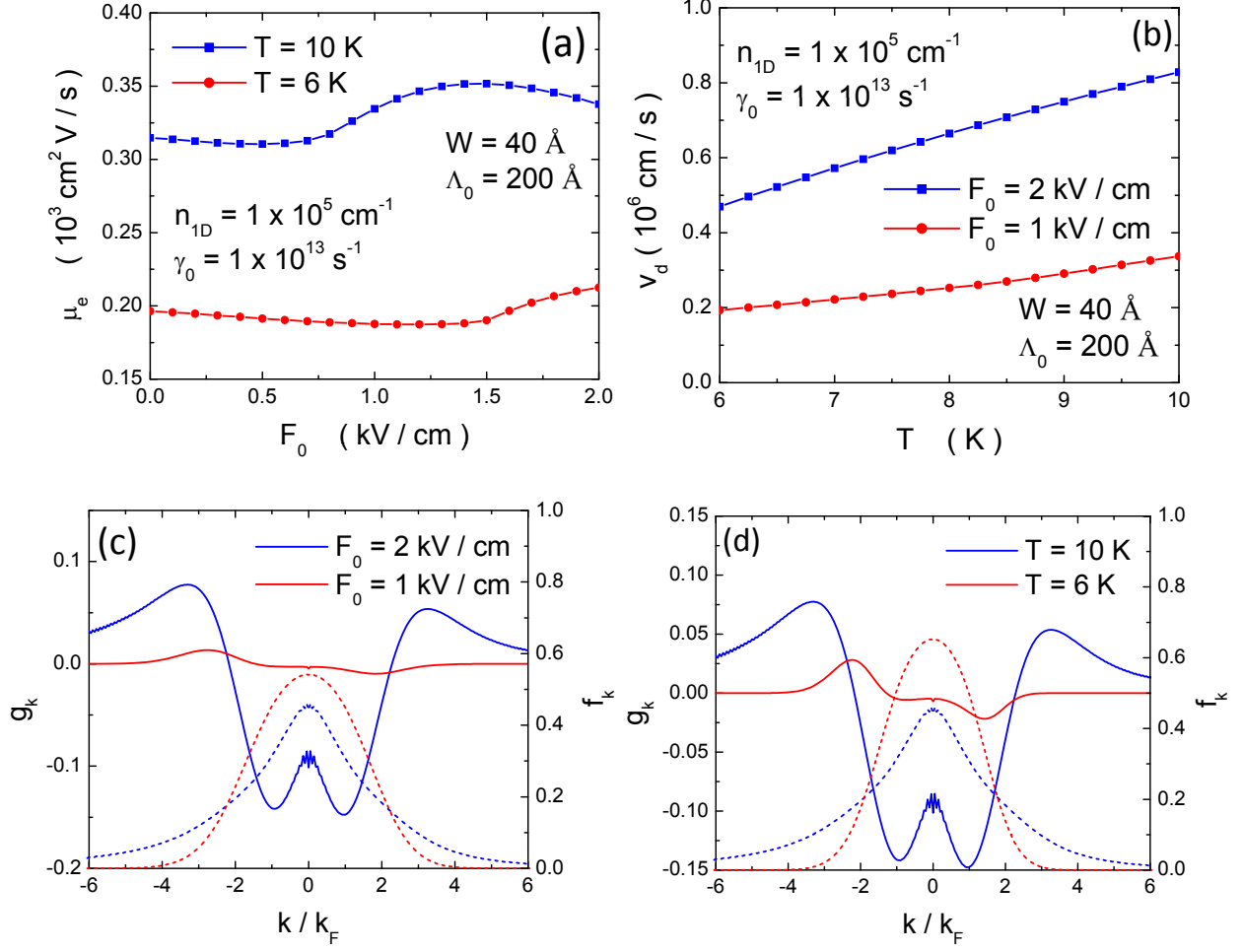


FIG. 2: (Color online) (a) Calculated electron mobilities μ_e as a function of applied electric field \mathcal{F}_0 at $T = 10 \text{ K}$ (solid squares on blue curve) and $T = 6 \text{ K}$ (solid circles on red curve); (b) Electron drift velocities v_d as a function of temperature T at $\mathcal{F}_0 = 2 \text{ kV/cm}$ (blue curve) and $\mathcal{F}_0 = 1 \text{ kV/cm}$ (red curve); (c) Non-equilibrium part of (g_k , left-hand scaled solid curves) and total (f_k , right-hand scaled dashed curves) electron distribution functions at $T = 10 \text{ K}$ as functions of electron wave number k along the ribbon with $\mathcal{F}_0 = 2 \text{ kV/cm}$ (blue curves) and $\mathcal{F}_0 = 1 \text{ kV/cm}$ (red curves); (d) g_k (left-hand scaled solid curves) and f_k (right-hand scaled dashed curves) with $\mathcal{F}_0 = 2 \text{ kV/cm}$ as functions of k at $T = 10 \text{ K}$ (blue curves) and $T = 6 \text{ K}$ (red curves). The other parameters are indicated directly in (a) and (b).

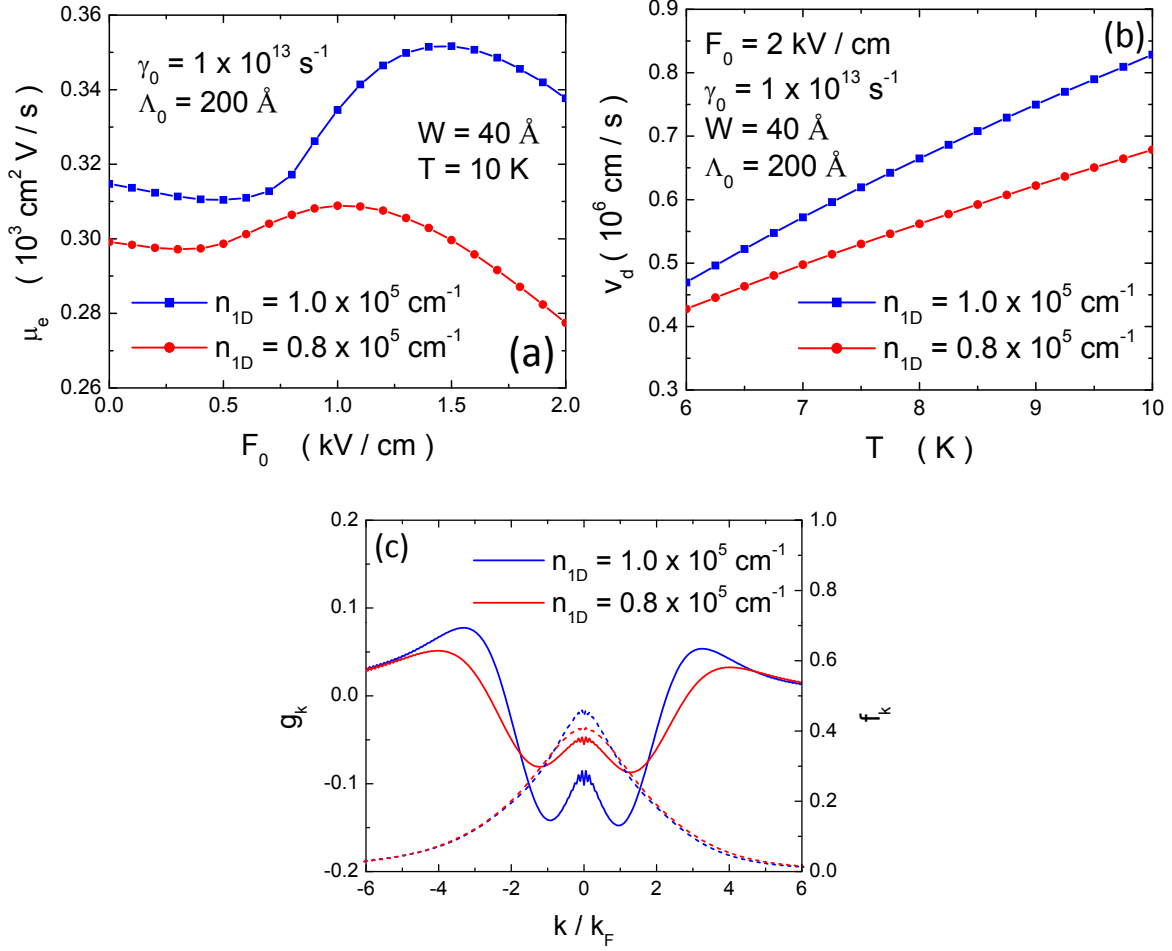


FIG. 3: (Color online) (a) Calculated μ_e as a function of \mathcal{F}_0 at $T = 10 \text{ K}$ with $n_{1D} = 1.0 \times 10^5 \text{ cm}^{-1}$ (solid squares on blue curve) and $n_{1D} = 0.8 \times 10^5 \text{ cm}^{-1}$ (solid circles on red curve); (b) v_d as a function of T with $\mathcal{F}_0 = 2 \text{ kV/cm}$ for $n_{1D} = 1.0 \times 10^5 \text{ cm}^{-1}$ (solid squares on blue curve) and $n_{1D} = 0.8 \times 10^5 \text{ cm}^{-1}$ (solid circles on red curve); (c) g_k (left-hand scaled solid curves) and f_k (right-hand scaled dashed curves) as a function of k . Here, the cases with $n_{1D} = 1.0 \times 10^5 \text{ cm}^{-1}$ and $n_{1D} = 0.8 \times 10^5 \text{ cm}^{-1}$ are represented by blue and red curves, respectively. The other parameters are indicated in (a) and (b).

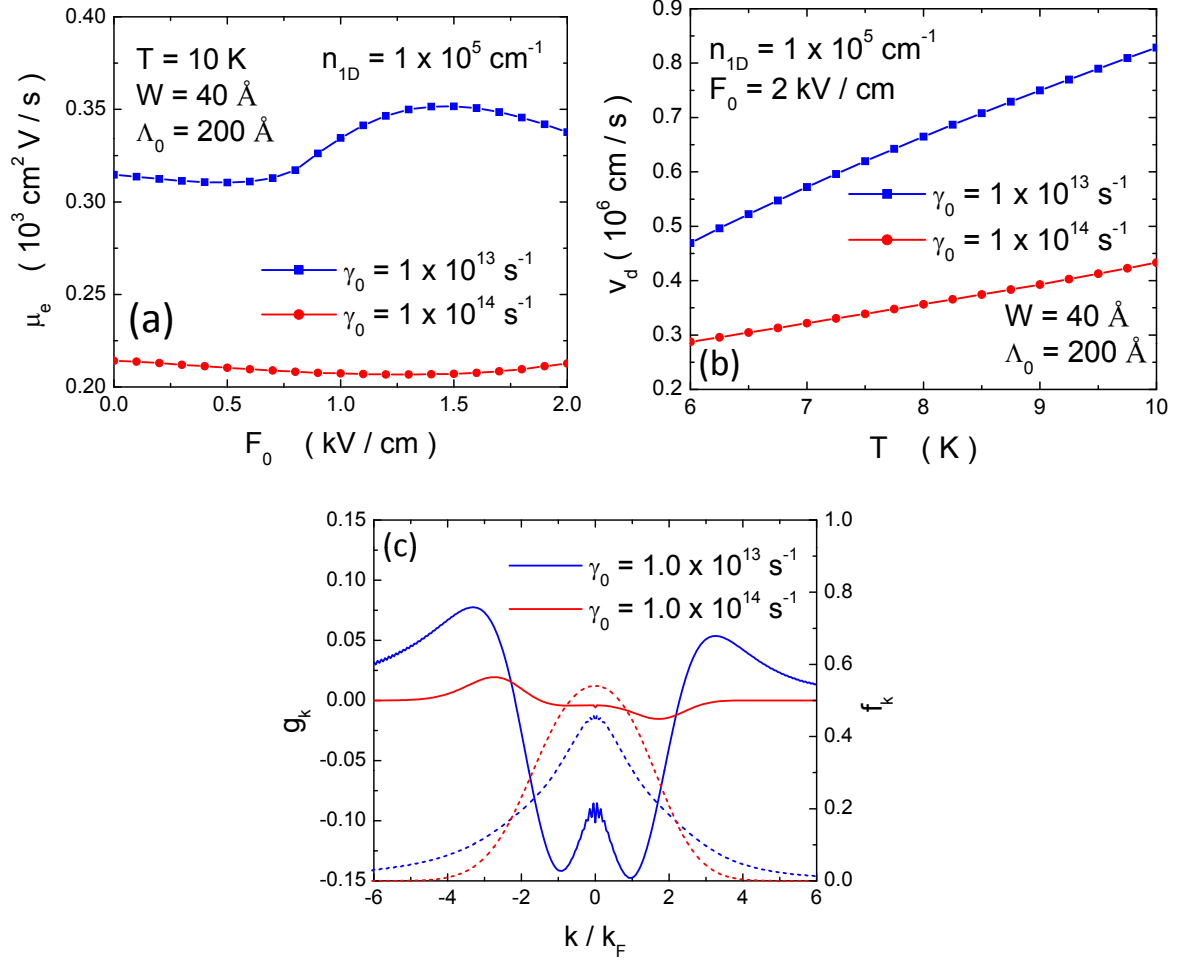


FIG. 4: (Color online) (a) μ_e as a function of \mathcal{F}_0 at $T = 10 \text{ K}$ with $\gamma_0 = 1.0 \times 10^{13} \text{ s}^{-1}$ (solid squares on blue curve) and $\gamma_0 = 1.0 \times 10^{14} \text{ s}^{-1}$ (solid circles on red curve); (b) v_d as a function of T with $\mathcal{F}_0 = 2 \text{ kV/cm}$ for $\gamma_0 = 1.0 \times 10^{13} \text{ s}^{-1}$ (solid squares on blue curve) and $\gamma_0 = 1.0 \times 10^{14} \text{ s}^{-1}$ (solid circles on red curve); (c) g_k (left-hand scaled solid curves) and f_k (right-hand scaled dashed curves) as a function of k . Here, the cases with $\gamma_0 = 1.0 \times 10^{13} \text{ s}^{-1}$ and $\gamma_0 = 1.0 \times 10^{14} \text{ s}^{-1}$ are represented by blue and red curves, respectively. The other parameters are indicated in (a) and (b).

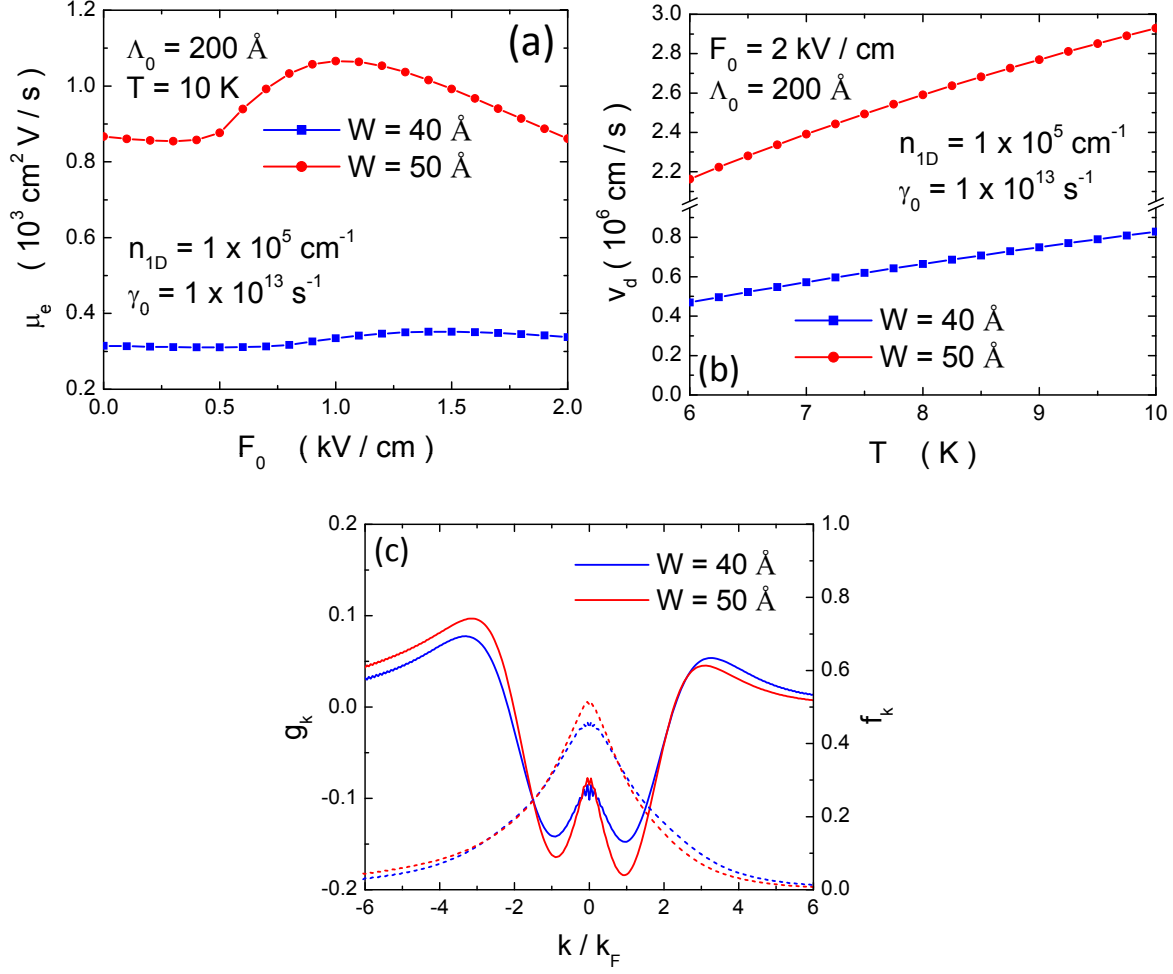


FIG. 5: (Color online) (a) μ_e as a function of \mathcal{F}_0 at $T = 10$ K with $W = 40$ Å (solid squares on blue curve) and $W = 50$ Å (solid circles on red curve); (b) v_d as a function of T with $\mathcal{F}_0 = 2$ kV/cm for $W = 40$ Å (solid squares on blue curve) and $W = 50$ Å (solid circles on red curve); (c) g_k (left-hand scaled solid curves) and f_k (right-hand scaled dashed curves) as a function of k . Here, the cases with $W = 40$ Å and $W = 50$ Å are represented by blue and red curves, respectively. The other parameters are indicated in (a) and (b).

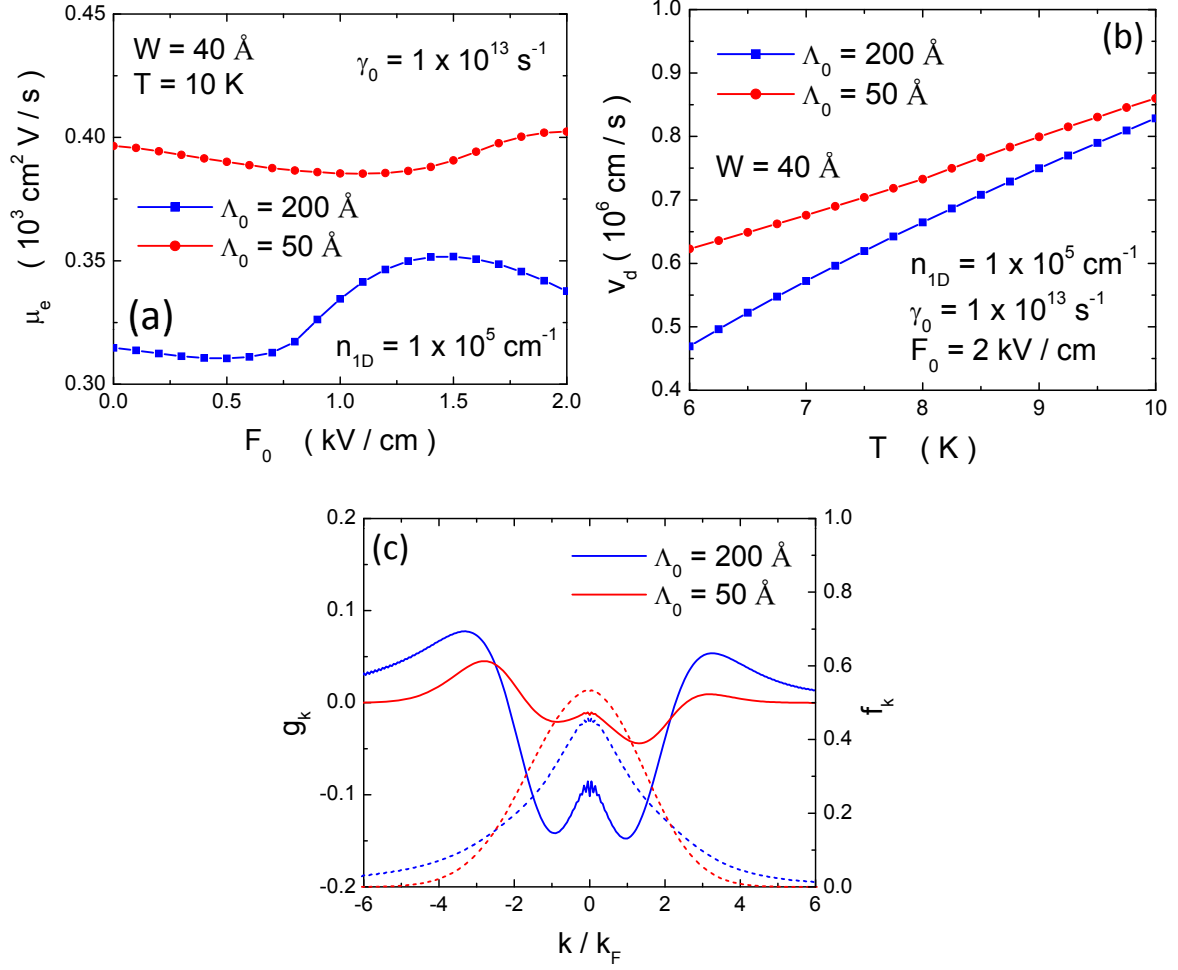


FIG. 6: (Color online) (a) μ_e as a function of \mathcal{F}_0 at $T = 10 \text{ K}$ with $\Lambda_0 = 200 \text{ \AA}$ (solid squares on blue curve) and $\Lambda_0 = 50 \text{ \AA}$ (solid circles on red curve); (b) v_d as a function of T with $\mathcal{F}_0 = 2 \text{ kV/cm}$ for $\Lambda_0 = 200 \text{ \AA}$ (solid squares on blue curve) and $\Lambda_0 = 50 \text{ \AA}$ (solid circles on red curve); (c) g_k (left-hand scaled solid curves) and f_k (right-hand scaled dashed curves) as a function of k . Here, the cases with $\Lambda_0 = 200 \text{ \AA}$ and $\Lambda_0 = 50 \text{ \AA}$ are represented by blue and red curves, respectively. The other parameters are indicated in (a) and (b).